SUPPORTING INFORMATION APPENDIX (SI Appendix)

21st Century Alchemy: Cupriphication of Gold to Sensitize d^{10}-d^{10} Metal-Metal Bonds and Near-Unity Phosphorescence Quantum Yields

Short title**:** Covalent d^{10}-d^{10} Bonds with ~100% Quantum Yields

Rossana Galassi,[a,*,#] Mukunda M. Ghimire,[b,#] Brooke M. Otten,[b,] Simone Ricci,[a] Roy N. McDougald Jr.,[b] Ruaa M. Almotawa,[b] Dieaa Alhmoud,[c] Joshua F. Ivy,[b] Abdel-Monem M. Rawashdeh,[c,*] Vladimir N. Nesterov,[b] Eric W. Reinheimer,[d] Lee M. Daniels,[d] Alfredo Burini,[a,*] and Mohammad A. Omary[b,c,*]

[a] School of Science and Technology, Chemistry Division, University of Camerino, *via* Sant'Agostino, 1, Camerino, I-62032, Italy; [b] Department of Chemistry, University of North Texas, Denton, Texas 76203, USA; [c] Department of Chemistry, Yarmouk University, Irbid, Jordan; [d] Rigaku Oxford Diffraction, 9009 New Trails Drive, The Woodlands, Texas, 77381-5209, USA

*To whom correspondence should be addressed. Email: omary@unt.edu (M.A.O.); alfredo.burini@unicam.it (A.B.); rossana.galassi@unicam.it (R.G.)

Author Contributions: All authors have contributed significantly to this manuscript. [#]R.G., M.M.G., and B.M.O. have contributed equally.

Conflict of Interest: None.

Keywords: Heterobimetallic Complexes; Cu(I)-Au(I) Complexes; d^{10}-d^{10} Metal-Metal Bonds; Near-Unity Photoluminescence Quantum Yields; OLED/LED Materials.

Experimental and Computational Methods

Materials and Experimental Methods

The starting complexes $[Cu(\mu\text{-}3,5\text{-}(CF_3)_2Pz)]_3$, $[Au(\mu\text{-}C^2,N^3\text{-}BzIm)]_3$,$[Au(\mu\text{-}C^2,N^3\text{-}MeIm)]_3$ and $[Au(\mu\text{-}C^2,N^3\text{-}EtIm)]_3$ were prepared by following a procedure described in the literature.(1,2) Solvents were purchased from Aldrich and distilled with conventional drying agents. All glassware was oven-dried at 150 °C overnight prior to use. Synthetic manipulations were carried out under a purified nitrogen atmosphere using standard Schlenk techniques. ^1H NMR spectra were recorded on an Oxford-400 Varian spectrometer (400.4 MHz for ^1H). Chemical shifts, in ppm, for the ^1H NMR spectra are relative to an internal Me_4Si standard. Elemental analyses (C, H, and N) were performed in-house with a Fisons Instruments 1108 CHNS-O Elemental Analyzer. Melting points were taken on an SMP3 Stuart Scientific Instrument. IR spectra were recorded from 4000 to 600 cm^{-1} with a Perkin-Elmer SPECTRUM ONE System FT-IR instrument; the far-IR measurements were carried out using a Nicolet 6700 Analytical FTIR Spectrometer equipped with a Smart Orbit high-performance diamond single bounce accessory for attenuated total reflectance (ATR) measurements on neat powder samples. IR annotations used: br = broad, m = medium, s = strong, sh = shoulder, w = weak.

Synthesis of $[Au_2(\mu\text{-}C^2,N^3\text{-}BzIm)_2Cu(\mu\text{-}3,5\text{-}(CF_3)_2Pz)]$, (1)

To a stirring dichloromethane (4 mL) solution of $[Au(\mu\text{-}C^2,N^3\text{-}BzIm)]_3$ (0.080 g; 0.075 mmol), solid $[Cu(\mu\text{-}3,5\text{-}(CF_3)_2Pz)]_3$ (0.030 g: 0.037 mmol) was added. The resulting colorless solution was stirred for 2 hours. X-ray diffraction quality single crystals were grown together with a white microcrystalline powder during the slow diffusion of hexane into the dichloromethane mixture reaction. The product isolated was not soluble in most organic solvents. Yield: 80%. M.p. 235 °C with decomposition. IR (cm^{-1}): 3133 (w), 3064 (w), 3030 (w), 1541 (m), 1507 (m), 1495 (m), 1441 (m), 1415 (m), 1389 (m), 1351 (m), 1267 (s), 1241 (m), 1163 (m), 1127 (vs), 1031 (s), 991 (m), 817 (m), 787 (w), 759 (m), 729 (m), 707 (s), 685 (m), 628 (m). Elemental analysis for $C_{25}H_{19}Au_2CuF_6N_6$: Calc'd. C, 30.80%; H, 1.96%; N, 8.62%. Found: C, 30.44%; H, 1.85%; N, 8.23%.

Synthesis of [Au(μ-C^2,N^3-BzIm)]$_3$[Cu(μ-3,5-(CF$_3$)$_2$Pz)]$_3$, (2)

To a stirring dichloromethane (4 mL) solution of [Cu(μ-3,5-(CF$_3$)$_2$Pz)]$_3$ (0.040 g; 0.050 mmol), solid [Au(μ-C^2,N^3-BzIm)]$_3$ (0.026 g; 0.025 mmol) was added. The colorless solution was stirred for 2 hours then 3 mL of hexane was layered on top. After a few days a white powder was collected. The crude product was washed with hexane (2 x 3 mL) and dichloromethane (2 x 2 mL) to eliminate traces of the starting materials. Yield 70%. M.p. 245 °C with decomposition. ^{1}H-NMR (CD_2Cl_2. 298 K): δ 7.30 – 7.23 (m, 15 H, C_6H_5), 6.98 (s, 3H, pzC*H*), 6.82 (s, 3H, 4-ImC*H*) 6.56 (s, 3H, 5-ImC*H*), 5.26 (s, 6H, CH_2-Im). IR (cm^{-1}): 3151 (w), 3063 (w), 3031 (w), 2928 (w), 1606 (w), 1549 (m), 1533 (m), 1508 (m), 1497 (m), 1446 (m), 1416 (m), 1363 (m), 1261 (s), 1227 (s), 1131 (vs), 1123 (vs), 991 (m), 902 m), 813 (m), 771 (m), 758 (m), 719 (s), 709 (s) 692 (m), 680 (m). Elemental analysis for $C_{45}H_{30}Au_3Cu_3F_{18}N_{12}$: Calc'd.: C, 29.02%; H, 1.62%; N, 9.03%. Found: C, 28.94%; H, 1.44%; N, 8.52%.

Synthesis of [Au$_2$(μ-C^2,N^3-MeIm)$_2$Cu(μ-3,5-(CF$_3$)$_2$Pz)], (3a)

Separately, 0.043 g (0.052 mmol) of [Au(μ-C^2,N^3-MeIm)]$_3$ was dissolved in 2 mL of dichloromethane and 0.021 g (0.026 mmol) of [Cu(μ-3,5-(CF$_3$)$_2$Pz)]$_3$ was dissolved in 2 mL of dichloromethane. The latter solution was transferred by cannula into the solution containing the gold metallocycle. After few minutes, a white precipitate formed and the resulting suspension was stirred for 2 hours. The white precipitate (**3b**) was filtered and washed with hexane (2 x 2 mL). The remaining dichloromethane solution was exposed to hexane vapors and after 3 weeks white crystals of (**3a**) suitable for X-ray diffraction were obtained. Yield 25%. M.p. 190 °C with decomposition. IR (cm^{-1}): 3161 (w), 3128 (w), 2948 (w), 1644 (w), 1532 (m), 1507 (m), 1407 (m), 1376 (m), 1263 (s), 1232 (sh), 1119 (vs), 1030 (s), 991 (m), 815 (s), 758 (m), 714 (s), 694 (m), 679 (m). Elemental analysis for $C_{13}H_{11}Au_2CuF_6N_6$ Calc'd.: C, 18.98%; H, 1.35%; N, 10.21%. Found: C, 19.29%; H, 1.10%; N, 9.70%.

Synthesis of [Au(μ-C^2,N^3-MeIm)Cu$_2$(μ-3,5-(CF$_3$)$_2$Pz)$_2$], (3b)

Separately, 0.040 g (0.050 mmol) of [Cu(μ-3,5-(CF$_3$)$_2$Pz)]$_3$ was dissolved in 2 mL of dichloromethane and 0.021 g (0.025 mmol) of [Au(μ-C^2,N^3-MeIm)]$_3$ was dissolved in 2 mL of dichloromethane. The latter solution was transferred by cannula into the solution containing the copper metallocycle. After few minutes, a white precipitate formed and the mixture was stirred for

2 hours. The white precipitate was filtered and washed with hexane (2 x 2 mL) to give the analytical sample **3b**. Yield 45%. M.p. 228.6 – 230 °C with decomposition. IR (cm^{-1}): 3148 (m), 3130 (sh), 2963 (m), 1662 (w), 1622 (w), 1548 (m), 1536 (sh), 1506 (m), 1446 (m), 1409 (m), 1380 (m), 1364 (m), 1258 (s), 1219 (s), 1118 (vs), 1029 (vs), 989 (m), 967 (m), 803 (m), 759 (m), 726 (s), 708 (m), 694 (m), 677 (m). Elemental analysis for $C_{14}H_7AuCu_2F_{12}N_6$ Calc'd.: C, 20.73%; H, 0.87%; N, 10.36%. Found: C, 20.16%; H, 0.64%; N, 9.96%.

Synthesis of [Au_4(μ-C^2,N^3-EtIm)$_4$$Cu_2$(μ-3,5-$(CF_3)_2$Pz)$_2$], (4a)

Separately, 0.050 g (0.060 mmol) of [Au(μ-C^2,N^3-EtIm)]$_3$ was dissolved in 2 mL of dichloromethane and 0.024 g (0.030 mmol) of [Cu(μ-3,5-$(CF_3)_2$Pz)]$_3$ was dissolved in 2 mL of dichloromethane. The latter solution was transferred by cannula into the solution containing the gold metallocycle. After few minutes, a white precipitate formed and the resulting suspension was stirred for 2 hours. The white precipitate (**4a**) was filtered and washed with hexane (2 × 2 mL). The remaining dichloromethane solution was left for slow evaporation and after a week yellowish white crystals of (**4a**) suitable for X-ray diffraction were obtained. Yield 75 %. M.p. 170 °C with decomposition. IR (cm^{-1}): 3152 (w), 3124 (w), 2921 (w), 2852(w) 1582 (w), 1539 (m), 1503 (w), 1463(m), 1447 (m), 1418(w), 1374(w) 1259 (s), 1231 (sh), 1124 (vs), 1029 (s), 990 (m), 811 (s), 757 (m), 713 (s), 683 (m).

Synthesis of [Au(μ-C^2,N^3-EtIm)Cu_2(μ-3,5-$(CF_3)_2$Pz)$_2$], (4b)

Separately, 0.050 g (0.063 mmol) of [Cu(μ-3,5-$(CF_3)_2$Pz)]$_3$ was dissolved in 2 mL of dichloromethane and 0.026 g (0.031 mmol) of [Au(μ-C^2,N^3-EtIm)]$_3$ was dissolved in 2 mL of dichloromethane. The latter solution was transferred by cannula into the solution containing the copper metallocycle. After few minutes, a white precipitate formed and the mixture was stirred for 2 hours. The white precipitate was filtered and washed with hexane (2 × 2 mL) to give the analytical sample **4b**. Yield 70%. M.p. 203°C with decomposition. IR (cm^{-1}): 3143 (w), 3128 (sh), 2923 (m), 2855(sh), 1582 (w), 1541 (w), 1507 (m), 1506 (m), 1461 (m), 1443 (m), 1412 (m), 1374 (m), 1258 (s), 1231 (s), 1123 (vs), 1027 (vs), 989 (m), 815 (m), 749 (m), 721 (s), 675 (m).

Luminescence Measurements

Photoluminescence studies have been carried out for all four complexes isolated in this work, namely **1**, **2**, **3a**, **3b, 4a**, and **4b**. The luminescence measurements were carried out for microcrystalline materials examined for purity for all four complexes and verified to represent the luminescence of the single crystals (which were examined with a hand-held dual-wavelength UV lamp) for complexes **3a** and **1**. Steady-state luminescence spectra were acquired with a PTI Quanta Master Model QM-4 scanning spectrofluorometer equipped with a 75-watt xenon lamp, emission and excitation monochromators, an excitation correction unit, a PMT detector, and an integrating sphere for direct quantum yield measurements. The emission and excitation spectra were corrected for the wavelength-dependent response of the detector and xenon arc lamp, respectively. Temperature-dependent studies were acquired with an Oxford optical cryostat using liquid nitrogen (down to 77 K) as a coolant. Lifetime data were acquired using a xenon flash lamp as a phosphorescence sub-system add-ons to the PTI instrument and the irradiation signal was de-convoluted using the resonance signal of the incident light upon the crystal. Processing of OLED thin films was performed *via* either vacuum sublimation of neat powders, utilizing a 12-source Trovato Model 300C vacuum deposition system, or drop-casting from nearly-saturated solutions of the two representative high-quantum-yield materials **3a** and $[Cu(\mu\text{-}3,5\text{-}(CF_3)_2Pz)]_3$.

X-Ray Crystallographic Determination

Crystal structure determination for compounds **1** and **3a** were carried out using a Bruker SMATR APEX2 CCD-based X-ray diffractometer equipped with a low temperature device and Mo-target X-ray tube (wavelength = 0.71073 Å). Measurements were taken at 100(2) K. Data collection, indexing, and initial cell refinements were carried out using APEX2, frame integration and final cell refinements were done using SAINT. An absorption correction was applied using the program SADABS. All non-hydrogen atoms were refined anisotropically. The hydrogen atoms in the compounds were placed in idealized positions and were refined as riding atoms. In both compounds the large residual electron density located close to the Au and Cu atoms (< 1.0 Å) is attributed to imperfect absorption corrections frequently encountered in heavy-metal atom structures. Structure solution, refinement, graphic and generation of publication materials were performed by using SHELXTL software. The final refinement of the **3a** crystal was performed using the Au : Cu ratio that was obtained from the elemental analysis (2 : 1).

Crystal structure determination for compound **4a** was carried out on a Rigaku Oxford Diffraction SuperNova X-ray diffractometer equipped with a Pilatus P200K Hybrid Photon Counting Detector. A pale yellow, plate-like crystal of dimensions 0.24 x 0.10 x 0.04 mm^3 was secured to a cryoloop using Paratone oil. Reflections were collected at 100(2) K using graphite-monochromated Mo $K_{\alpha 1}$ radiation (λ = 0.71073 Å) using a data collection strategy calculated within CrysAlis^{Pro} to ensure desired data redundancy and percent completeness. Unit cell determination, initial indexing, data collection, frame integration, Lorentz-polarization corrections and final cell parameter calculations were carried out using CrysAlis^{Pro}. A numerical absorption correction was performed using the SCALE3 ABSPACK algorithm embedded within CrysAlis^{Pro}. The structure was solved *via* the intrinsic phasing methodology using ShelXT,(3) refined using ShelXL(4) in the AutoChem 2.1 graphical user interface and had its space group unambiguously verified by PLATON.(5) The final structural refinement included anisotropic temperature factors on all non-hydrogen atoms. All hydrogen atoms were attached *via* the riding model at calculated positions using appropriate HFIX commands. Crystal data and refinement details are summarized in **Table S1** for **1**, **3a**, and **4a**.

Thin Film and Powder X-ray Diffraction (XRD) Analysis

For XRD analysis, the powder and thin film samples of **3a, 4a** and **Cu_3** were characterized at room temperature on Rigaku D/Max 2200PC Ultima III X-ray diffractometer using K-beta filtered Cu-Kα radiation (λ = 1.5406 Å). Glass substrates were used to analyze the powder sample whereas the thin films were prepared using quartz substrates by drop-casting saturated dichloromethane solutions. Simulated powder XRD patterns of single crystals were generated using Mercury software.

Computational Methodology

Geometry optimization and single-point calculations were performed for **4a** and derivatives thereof using the Gaussian 09 suite of programs. As opposed to the ubiquitous B3LYP hybrid functional, we elected to utilize the M06 meta-hybrid functional – in conjunction with the CEP-31G(d)(6,7) basis set where d signifies the addition of a d-polarization function to main group elements. Although other methods exist, we adopted M06 as recommended by Truhlar and co-workers to be most suitable as a universal density functional (dubbed "a desert island" functional

by Truhlar)(8,9) in the study of systems that may include significant non-covalent interactions, as needed herein to distinguish metallophilic/non-covalent Cu(I)···Au(I) and Au(I)···Au(I) interactions from polar-covalent Cu(I)-Au(I) bonds.

Table S1: Crystallographic Data and Refinement Parameters for **1**, **3a**, and **4a**

	Complex **1**	Complex **3a**	Complex **4a**
Empirical formula	C_{25} H_{19} Au_2 Cu F_6 N_6	C_{13} H_{11} Au_2 Cu F_6 N_6	$C_{30}H_{30}Au_4Cu_2F_{12}N_{12}$
Molecular weight	974.94	822.75	1701.60
Crystal system	Orthorhombic	Monoclinic	Triclinic
Space group	*Pbcn*	*C*2/*c*	*P-1*
a (Å)	27.205 (16)	19.094(2)	8.09925(14)
*b (*Å)	12.118 (7)	12.486 (1)	10.7781(2)
*c, (*Å)	7.937 (5)	7.8003(6)	12.8747(3)
α (°)	90	90	114.6079(19)
β (°)	90	102.329(1)	92.4118(16)
γ (°)	90	90	92.7737(15)
V (Å^3)	2617(3)	1816.7(3)	1018.22(4)
Z	4	4	1
T (K)	100(2)	100(2)	100(2)
ρ_{calcd} (mg/m^3)	2.475	3.008	2.775
μ (mm^{-1})	12.063	17.342	15.476
F(000)	1808	1488	776
Reflections collected	19771	10607	12099
Independent reflections	2317	1918	4155
R_{int}	0.1778	0.0260	0.0334
$^aR_1$ [$I > 2\sigma(I)$]	0.0508	0.0386	0.0235
$^bwR_2$ [$I > 2\sigma(I)$]	0.1152	0.0966	0.0507

$^a R_1 = \Sigma||F_o| - |F_c||/\Sigma|F_o|$. $^b {}_wR_2 = \{\Sigma[w(F_o{}^2 - wF_c{}^2)^2/\Sigma[w(F_o{}^2)^2]\}^{1/2}$

Table S2: Selected Bond Lengths (Å), Intramolecular Contacts (Å) and Angles (°) for **1**, **3a**, and **4a.**

Complex 1	
Au(1)-N(1)	2.079(11)
Au(1)-C(4)	2.007(14)
Au(1)···Au(1A)#1[a]	3.303(2)
Cu(1)-N(3)	1.860(12)
Cu(1)···Au(1)	3.432(2)
Cu(1)···Au(1A)#1[a]	3.432(2)
N(1)-Au(1)-C(4)	177.6(5)
Au(1)-C(4)-N(2)	126(1)
Au(1)-C(4)-N(3)	123(1)
N(3)-Cu(1)-N(3A)#1[a]	175.7(7)
Cu(1)-N(3)-C(4)	123(1)
Cu(1)-N(3)-C(6)	131(1)

Complex 3a	
Au(1)-C(4)	2.021(15)
Au(1)-N(1)	2.077(7)
Au(1)···Au(1A)#2[a]	3.253(7)
Au(1)···Cu(2)	3.510(7)
Cu(2)-N(2)	1.781(14)
C(4)-Au(1)-N(1)	175.4(4)
N(2A)#2a-Cu(2)-N(2)	168(1)
Cu(1)···Au(2)	3.501(7)
Cu(1)···Cu(1A)#2a	3.425(7)
Cu(1)-N(2')	1.91(3)
Cu(1)-N(1)	1.88(2)
Au(2)-C(4')	2.24(3)
C(4'A)-Au(2)-C(4')#2[a]	172(2)
N(2')-Cu(1)-N(1)	171(1)

Complex 4a	
Au(1)-Cu(1)‡	*2.8750(8)*
Au(1)···Au(2)‡	3.4883(8)
Au(1)···Au(2)*	3.4220(3)
Au(1)···Cu(1)*	3.3745(7)
Au(1)···Cu(2)*	3.3081(7)
Au(1)-C(13)	1.983(6)
Au(1)-N(1)	2.051(5)
Au(2)-C(3)	1.973(6)
Au(2)-N(3)	2.056(5)
Cu(1)-N(4)	1.889(5)
Cu(1)-N(5)	1.866(5)
N(5)-Cu(1)-N(4)	*167.5(2)*
C(13)-Au(1)-N(1)	173.4(2)
C(3)-Au(2)-N(3)	176.4(2)
C(8)-N(4)-Cu(1)	131.2(4)
C(11)-N(5)-Cu(1)	130.6(4)
C(13)-N(5)-Cu(1)	121.0(4)
C(3)-N(1)-Au(1)	117.3(4)
C(1)-N(1)-Au(1)	133.8(4)
N(5)-C(13)-Au(1)	122.1(4)
N(6)-C(13)-Au(1)	130.9(4)
C(6)-N(3)-Au(2)	133.6(4)

[a]Symmetry transformations to generate equivalent atoms: #1 -x+1, y,-z+3/2; #2: -x + 1, y, -z +1/2. ‡Intermolecular separation. *Intramolecular separation.

Table S3. Morse Potential Fitting (MPF) and Dunham Analysis (DA) of Selected Vibrational Frequencies in the Full $\{[Au_2Im'_2CuPz')]\}_2$ Hexanuclear Dimer-of-Trimer (DOT) Model Upon Selected Vertical Vibrations in Its Two-Component Monomer-of-Trimer (MOT) Units.

Vibration	Method	μ *(a.u.)*	R_e *(Å)*	ω_e *(cm^{-1})*	$\omega_e x_e$ *(cm^{-1})*
$\nu_{Cu\leftrightarrow Au(symm)}$ in MOT $\leftrightarrow$ MOT	MPF	48*	2.9039	179	0.658
$\nu_{MOT\leftrightarrow MOT\ (symm)}$	MPF	425	2.9039	61.2	0.077
$\nu_{Cu\leftrightarrow Au(symm)}$ in MOT $\leftrightarrow$ MOT	DA	48*	2.9036	182.3	3.14
$\nu_{MOT\leftrightarrow MOT\ (symm)}$	DA	425	2.9036	61.3	0.35
Pure $\nu_{Cu\leftrightarrow Au(symm)}$	DA	48	2.9020	182.3	44.67
Pure $\nu_{Cu\rightarrow Au(asymm)}$	DA	48**	2.9019	172.7	31.8

*: Effective reduced mass assumed to be that of the Cu and Au atoms within the symmetric intertrimer vibration of the two entire MOT units. See vibrations designated "Pure" for analogous values from scan calculations whereby only the metal atoms were motioned in the intertrimer vibration while the rest of two MOT units remained stagnant.

**: Effective reduced mass assumed to be that of the Cu and Au atoms within the asymmetric intertrimer vibration whereby only the two Cu atoms were motioned towards the two corresponding Au atoms, which remained stagnant.

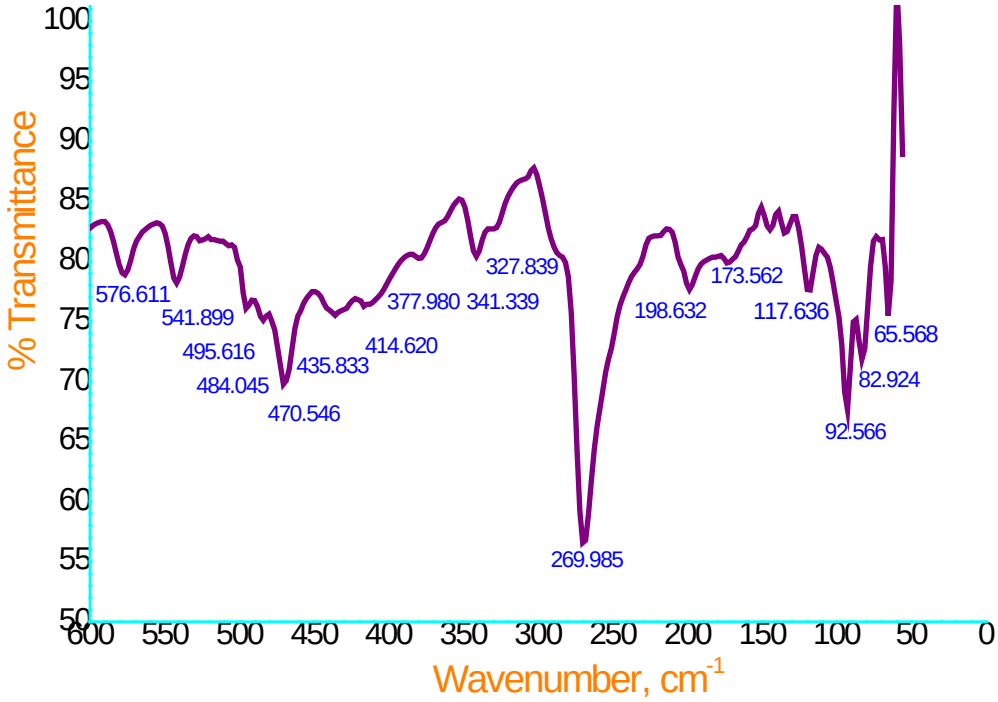

Fig. S1. Infrared spectrum of a neat solid powder of **4a** in the far-IR region. Most bands at < 200 cm^{-1} have significant $\nu_{Cu\text{-}Au}$ contribution based on animations and high reduced masses shown in the DFT simulations or based on the Gray-Harvey correlation method.

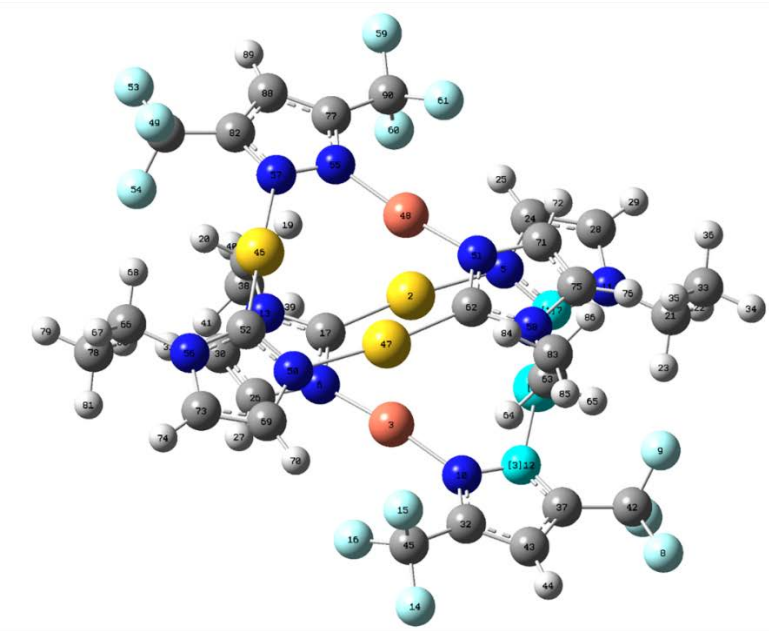

M06-Optimized	Length (Å)/Angle (°)
Au(2)-Cu(48)	2.9039
Cu(3)-Au(47)	2.9039
Cu(3)-Au(2)	3.5018
Cu(3)-Au(1)	3.3878
Cu(48)-Au(47)	3.5018
Cu(48)-Au(46)	3.3878
Cu(3)-N(6)	1.8810
Cu(3)-N(10)	1.9062
Au(2)-N(5)	2.1081
Au(2)-C(17)	2.0344
Au(1)-N(12)	2.1159
Au(1)-C(7)	2.0284
Cu(48)-N(51)	1.8810
Cu(48)-N(55)	1.9062
Au(47)-N(50)	2.1081
Au(47)-C(62)	2.0344
Au(46)-N(57)	2.1159
Au(46)-C(52)	2.0284
N(51)-Cu(40)-N(55)	171.0
N(50)-Au(47)-C(62)	172.8
N(57)-Au(46)-C(52)	176.7
N(6)-Cu(3)-N(10)	171.0
N(5)-Au(2)-N(5)	172.7
N(12)-Au(1)-N(12)	176.7

Fig. S2. Dispersive DFT (M06/CEP-31G(d)) optimized structure of **4a**.

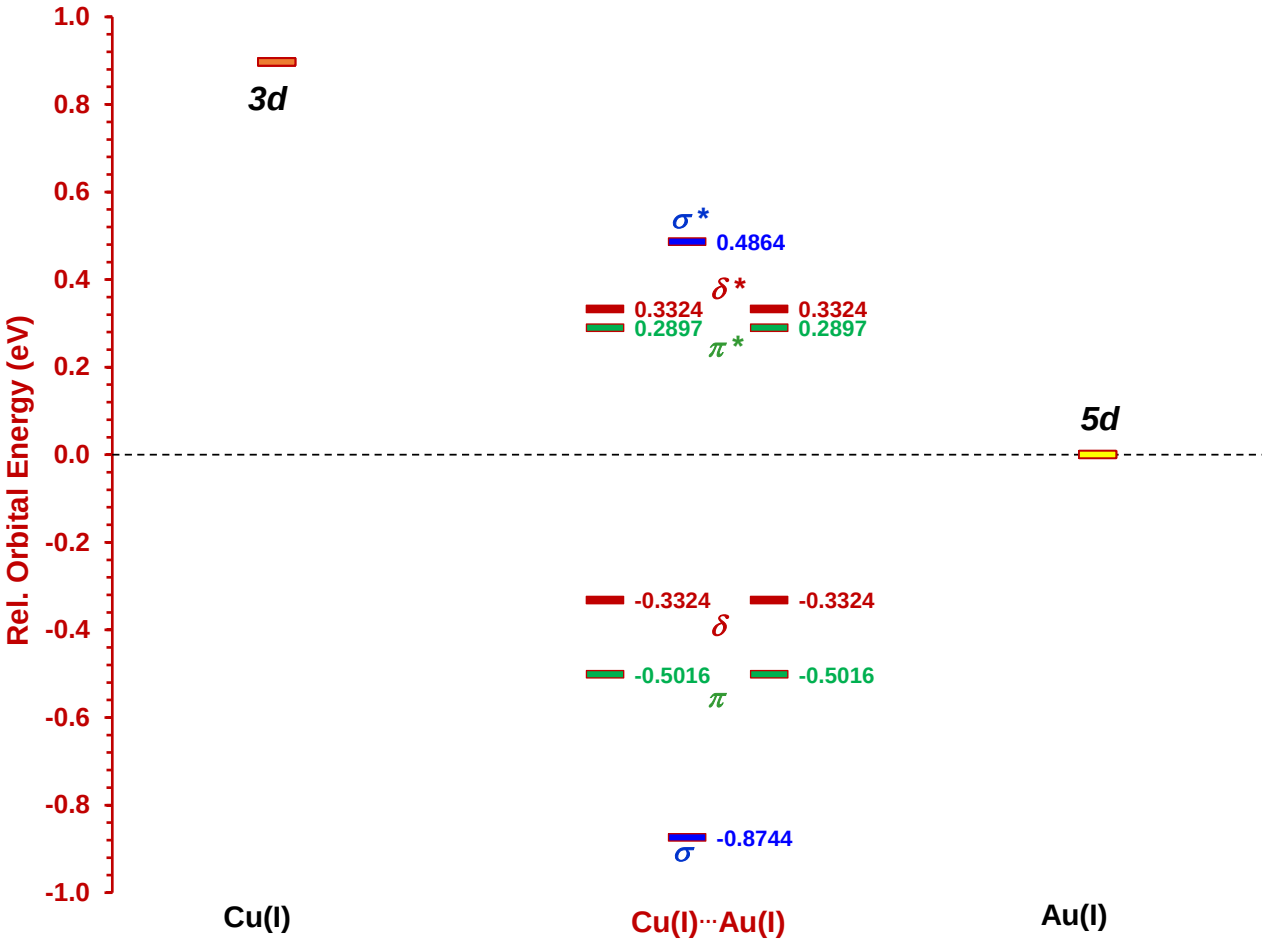

Scheme S1. Orbital mixing models that postulate Cu(I)···Au(I) polar-covalent metallophilic bonding formalism in an isolated $[CuAu]^{2+}$ diatomic unit. Orbital energies are taken from DFT computations at the crystallographic geometry of **4a** for the Cu(I)-Au(I) diatomic model. The asymmetric splitting of the σ and π orbitals is attributed to the lowering of the σ* and π* energy levels due to interaction with the 4s and 4p vacant orbitals of Cu(I); however, these (and δ*) remain anti-bonding in nature so the lowering is interpreted as metallophilic stabilization without increasing the formal bond order from zero in this naked $[CuAu]^{2+}$ heteronuclear diatomic model.

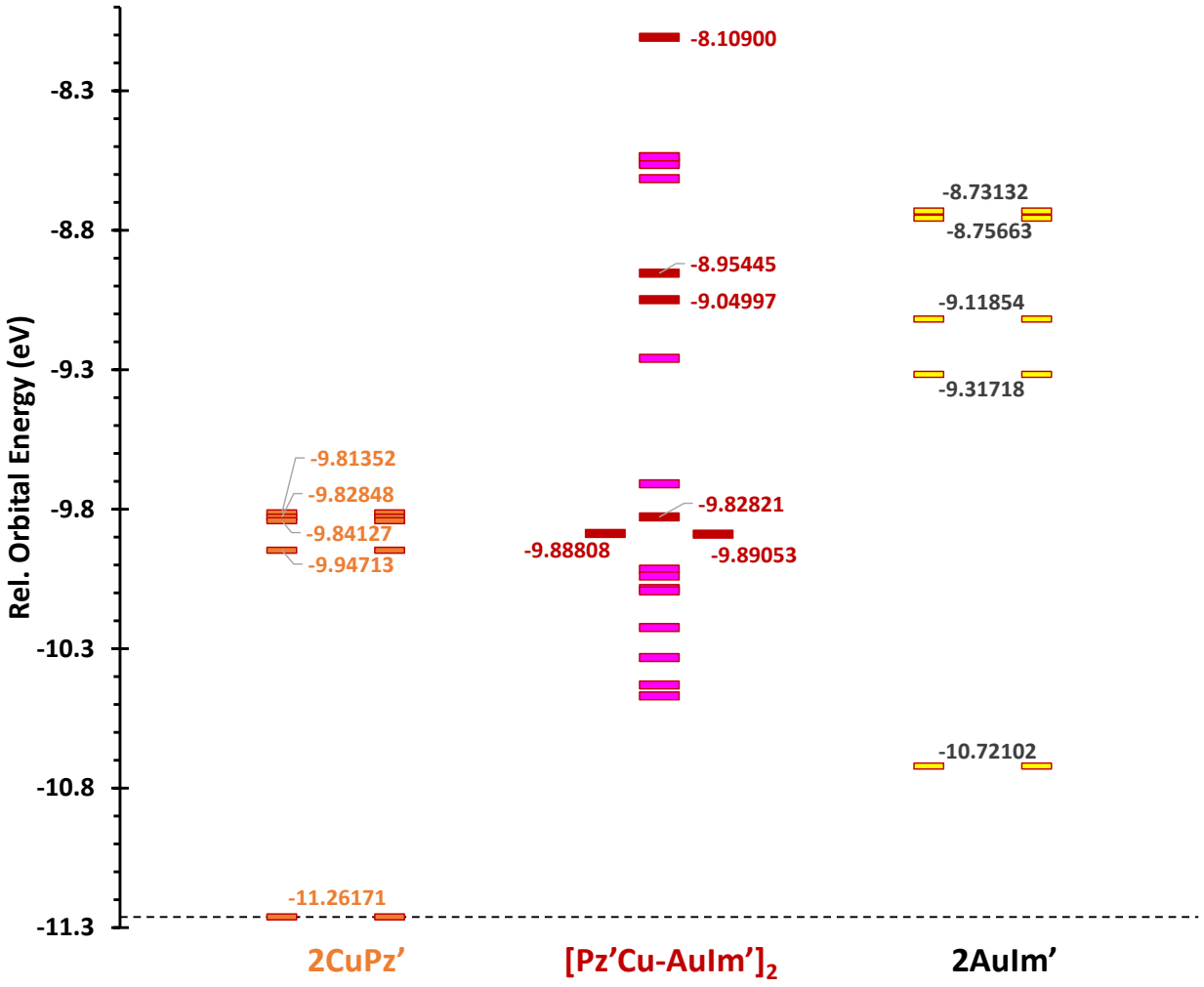
Rel. Orbital Energy (eV)
-8.3
-8.8
-9.3
-9.8
-10.3
-10.8
-11.3
-8.10900
-8.95445
-9.04997
-9.82821
-9.88808
-9.89053
-8.73132
-8.75663
-9.11854
-9.31718
-10.72102
-9.81352
-9.82848
-9.84127
-9.94713
-11.26171
2CuPz'
[Pz'Cu-AuIm']2
2AuIm'

(a)

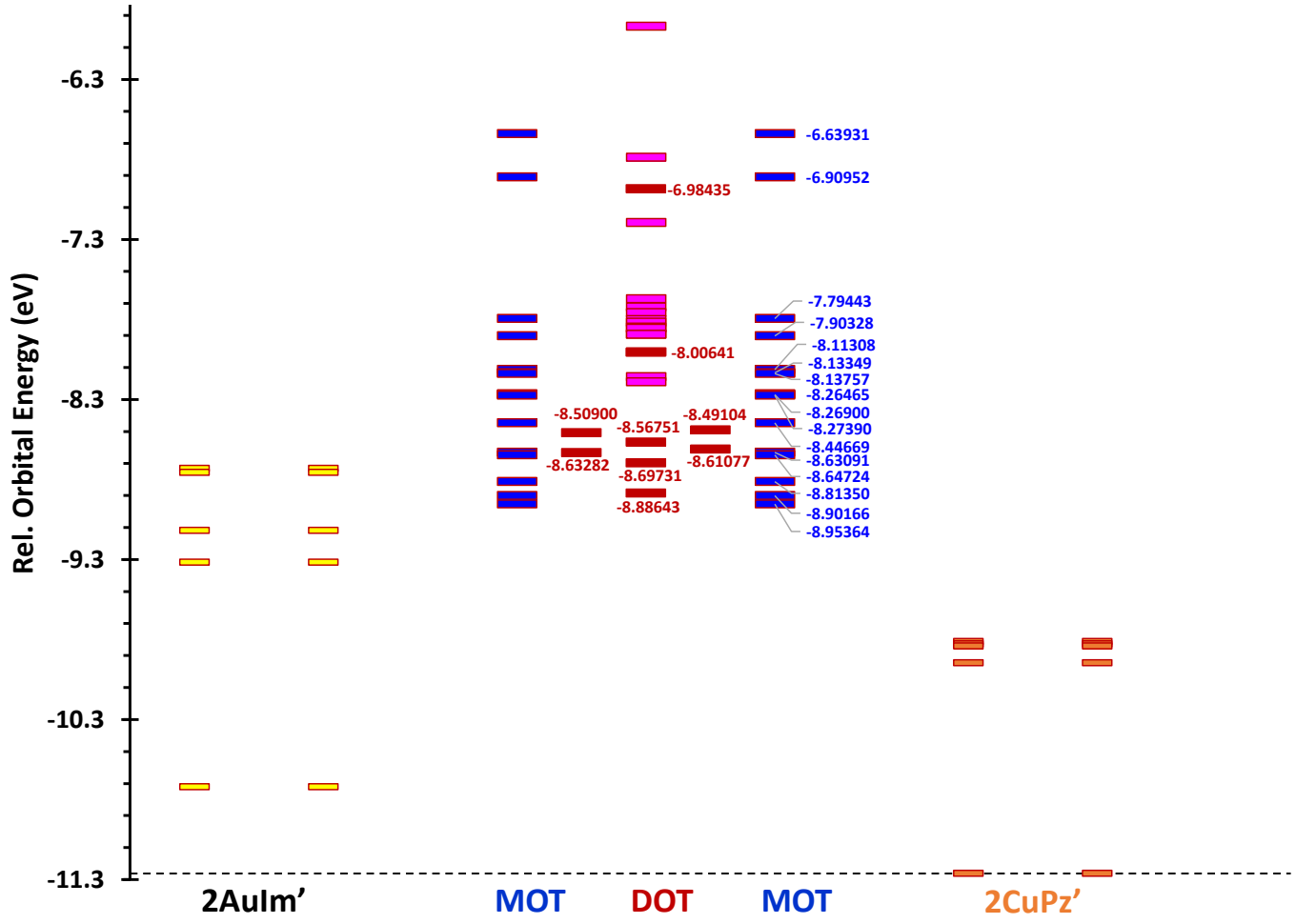

(b)

Scheme S2. Orbital mixing models that postulate Cu(I)-Au(I) polar-covalent bonding formalism of the Pz'Cu-AuIm' interaction in: **(a)** [Pz'Cu-AuIm']$_2$ tetranuclear cluster, and **(b)** the full {[Au$_2$Im'$_2$CuPz')]}$_2$ hexanuclear dimer-of-trimer (DOT), comprising two [Au$_2$Im'$_2$CuPz')] monomer-of-trimer (MOT) units, where Im' = μ-C^2,N^3-EtIm and Pz' = μ-3,5-(CF$_3$)$_2$Pz. Orbital energies are taken from DFT computations at the crystallographic geometry of **4a** for the [Pz'Cu-AuIm']$_2$ model and its CuPz' and AuIm' components but at the fully-optimized geometry of the MOT and full {[Au$_2$Im'$_2$CuPz')]}$_2$ hexanuclear DOT model. The strong orbital mixing of the d-based filled atomic orbitals with the 6s and 6p vacant orbitals of Au(I) as well as 4s and 4p vacant orbitals of Cu(I) in these ligand-containing models alter the nature of at least one formally anti-bonding orbital from the formalism in Scheme S1 above to render it bonding instead, resulting in a total of at least 6 strongly-bonding orbitals – instead of 5 – in both models (designated in maroon colors for orbital energy levels and labeled orbital energy values; see highlighted orbitals in **Fig.**

S3 below). The full hexanuclear DOT model exhibits 3 additional bonding orbitals due to additionally-strengthened (n+1) outer-shell orbital mixing for MOT molecular orbitals with d_{xy}, d_{x2-y2}, and (to a lesser extent) d_{z2} δ-character of each trigonal planar molecule; this results in 3 additional strongly-bonding orbitals for a total of 9 strongly-bonding orbitals in the hexanuclear DOT (designated in maroon colors for orbital energy levels and labeled orbital energy values; see highlighted orbitals in **Fig. S5** below as well as **Fig. 4** insets in the main manuscript).

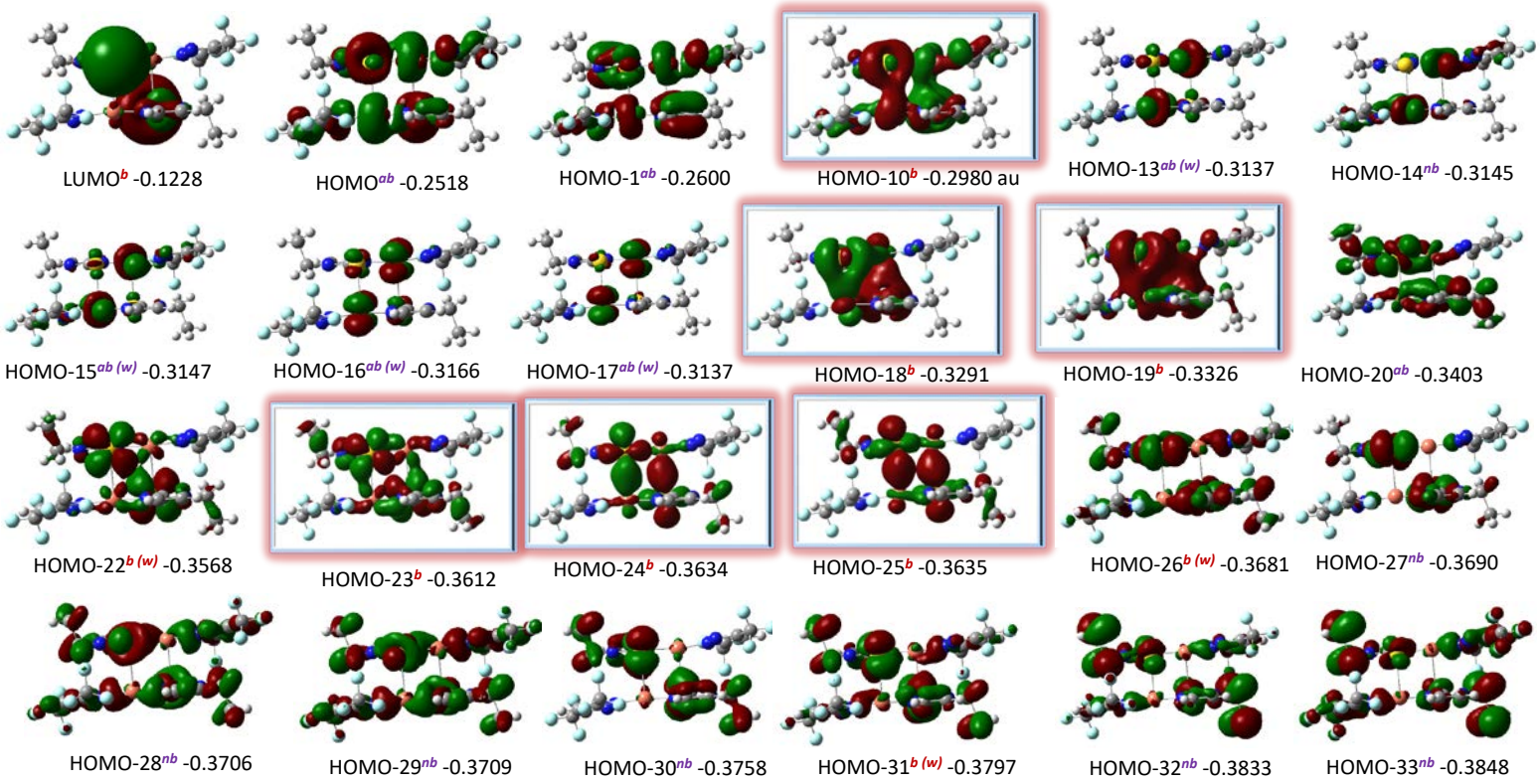

Fig. S3. Kohn-Sham contours of frontier molecular orbitals with significant electron density on metal atoms in a $[Cu_2Pz'_2Au_2Im'_2]$ tetranuclear cluster model, where Im' = μ-C^2,N^3-EtIm and Pz' = μ-3,5-$(CF_3)_2$Pz. Orbital energies are taken from DFT computations at the crystallographic geometry of **4a**. Orbital notation is given to describe both the relative energy (e.g., HOMO = highest occupied molecular orbital; HOMO-24 = the occupied molecular orbital that lies 24th below the HOMO) and absolute energy, given in atomic units next to orbital designations, as well as the Cu-Au bonding character (superscripts "b", "nb", "ab", and "ab (w)" indicate bonding, non-bonding, anti-bonding, and weakly- anti-bonding, respectively). The 6 occupied orbitals that exhibit a particularly strong Cu-Au bonding character are highlighted. The isodensity = 0.01 for all orbitals.

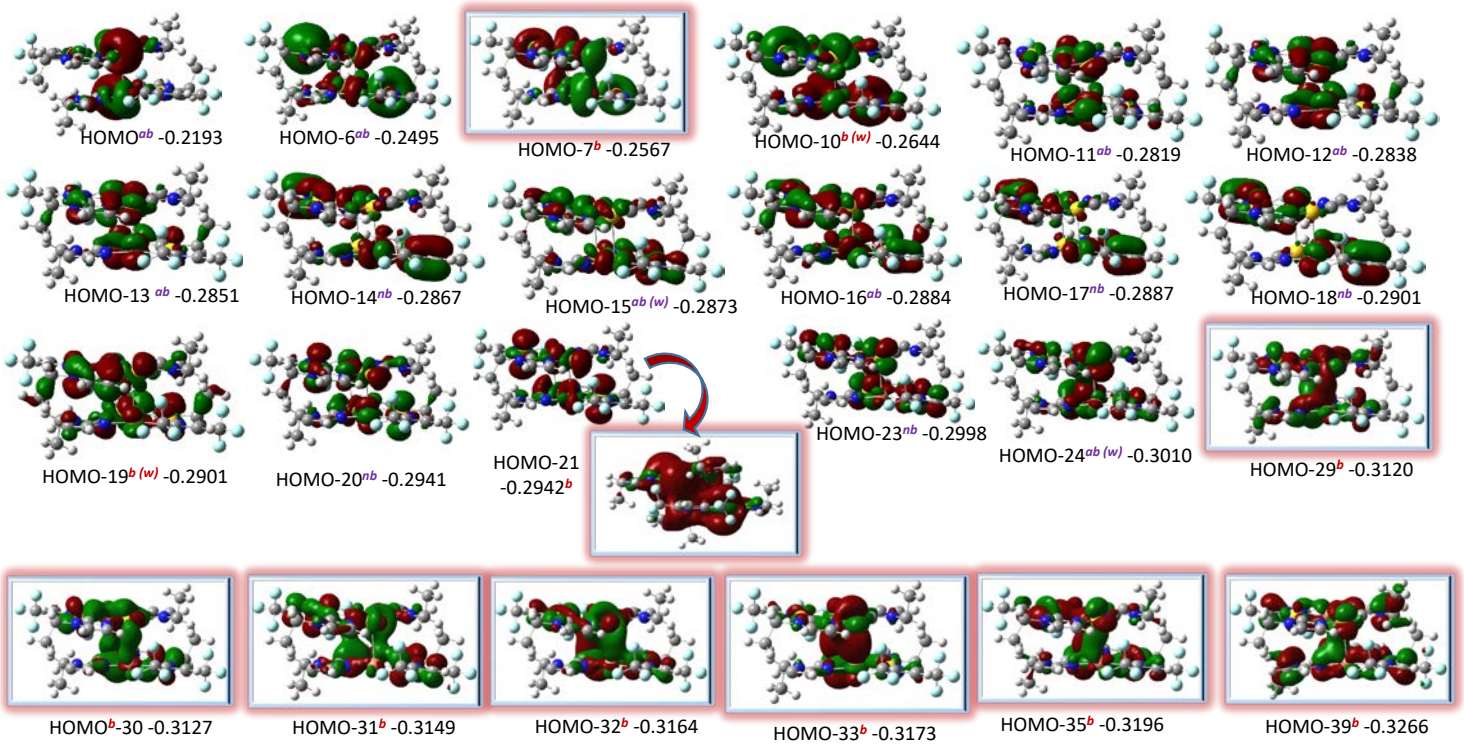

Fig. S4. Kohn-Sham contours of frontier molecular orbitals with significant electron density on metal atoms in the full $\{[Au_2Im'_2CuPz')]\}_2$ hexanuclear dimer-of-trimer model, where Im' = μ-C^2,N^3-EtIm and Pz' = μ-3,5-$(CF_3)_2$Pz. Orbital energies are taken from DFT computations of the optimized geometry of **4a** shown in **Fig. S2**. Orbital notation is given to describe both the relative energy (e.g., HOMO = highest occupied molecular orbital; HOMO-35 = the occupied molecular orbital that lies 35th below the HOMO) and absolute energy, given in atomic units next to orbital designations, as well as the Cu-Au bonding character (superscripts "b", "nb", "ab", and "ab (w)" indicate bonding, non-bonding, anti-bonding, and weakly- anti-bonding, respectively). The 9 occupied orbitals that exhibit a particularly strong intertrimer Cu-Au bonding character are highlighted. The isodensity = 0.01 for the zoomed out HOMO-21 and 0.02 for all other orbitals.

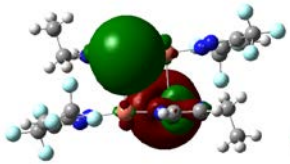

LUMO -0.1228

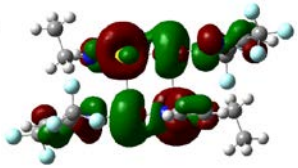

HOMO -0.2518

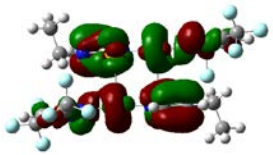

HOMO-1 -0.2600

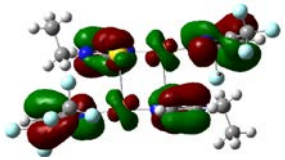

HOMO-2 -0.2654

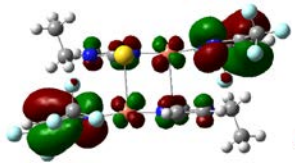

HOMO-3-0.2657

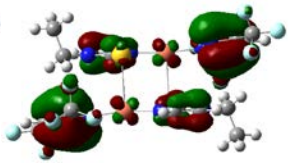

HOMO-4 -0.2694

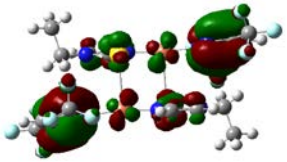

HOMO-5 -0.2706

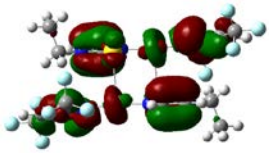

HOMO-6 -0.2743

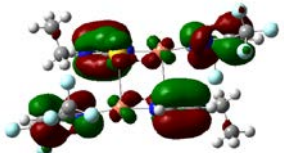

HOMO-7 -0.2748

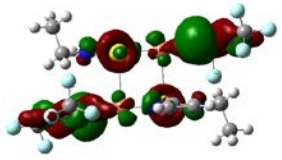

HOMO-8 -0.2856

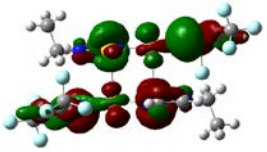

HOMO-9 -0.29115

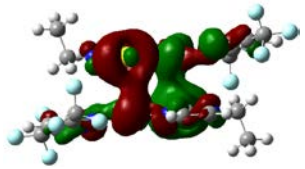

HOMO-10 -0.2980

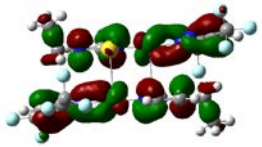

HOMO-11 -0.3060

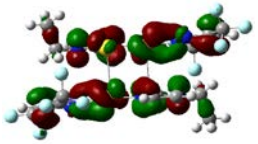

HOMO-12 -0.3104

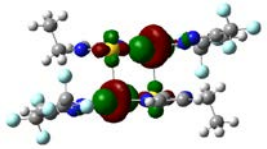

HOMO-13 -0.3137

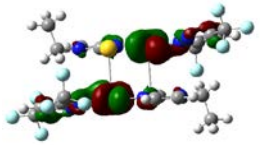

HOMO-14 -0.3145

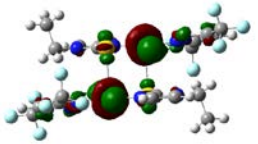

HOMO-15 -0.3147

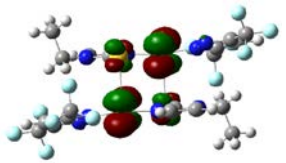

HOMO-16 -0.3166

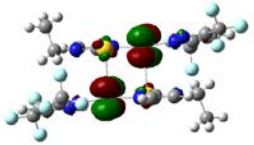

HOMO-17 -0.3137

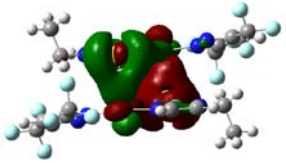

HOMO-18 -0.3291

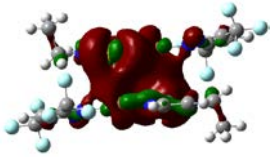

HOMO-19 -0.3326

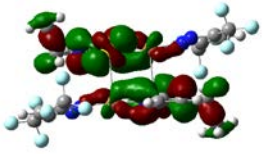

HOMO-20 -0.3403

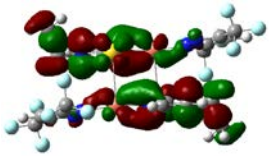

HOMO-21 -0.3408

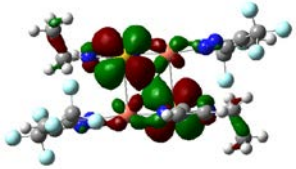

HOMO-22 -0.3568

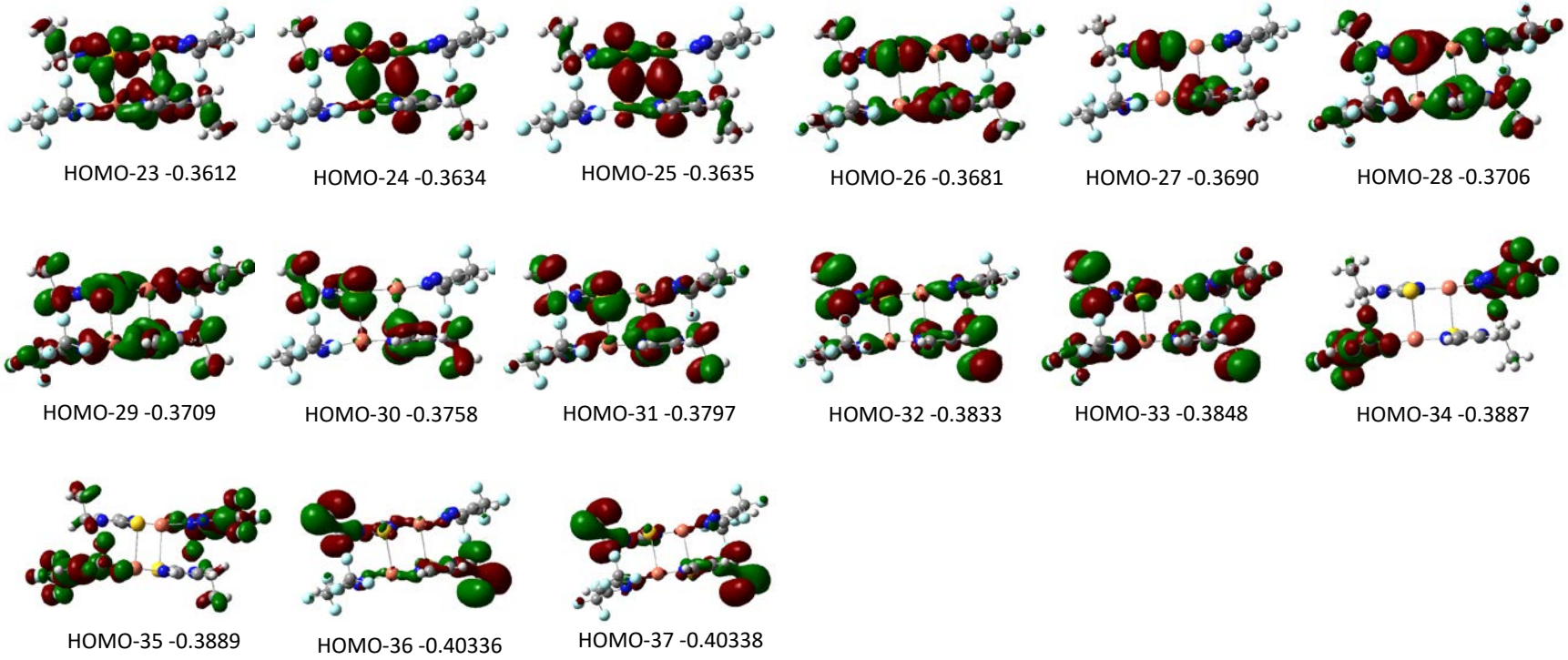

Fig. S5. Kohn-Sham contours of all occupied frontier molecular orbitals (from the HOMO down to HOMO-37) plus the lowest unoccupied molecular orbital (LUMO) in a [$Cu_2Pz'_2Au_2Im'_2$] tetranuclear cluster model, where Im' = μ-C^2,N^3-EtIm and Pz' = μ-3,5-$(CF_3)_2$Pz. Orbital energies are taken from DFT computations at the crystallographic geometry of **4a**. Orbital notation is given to describe both the relative energy (e.g., HOMO = highest occupied molecular orbital; HOMO-32 = the occupied molecular orbital that lies 32nd below the HOMO) and absolute energy, given in atomic units next to orbital designations. The isodensity = 0.01 for all orbitals.

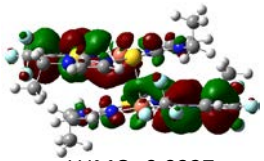
LUMO -0.0327

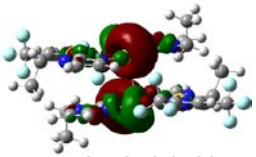
HOMO -0.2193

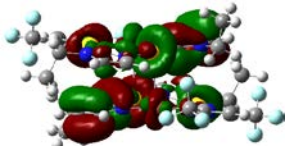
HOMO-1 -0.2208

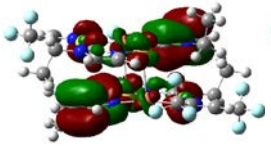
HOMO-2 -0.2288

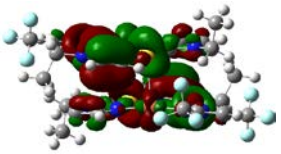
HOMO-3 -0.2309

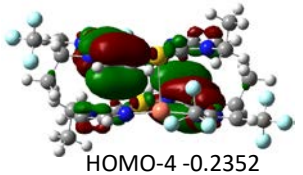
HOMO-4 -0.2352

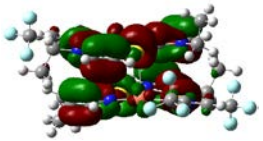
HOMO-5 -0.2417

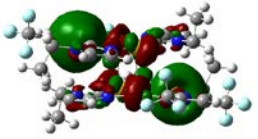
HOMO-6 -0.2495


HOMO-7 -0.2567

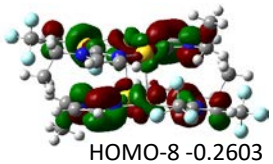
HOMO-8 -0.2603

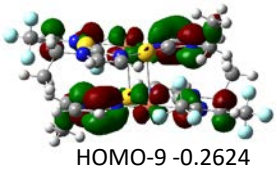
HOMO-9 -0.2624

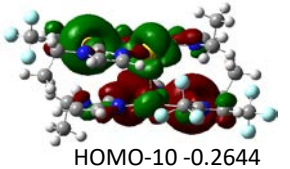
HOMO-10 -0.2644

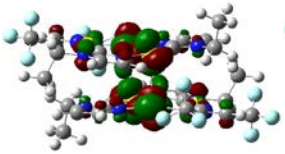
HOMO-11 -0.2819

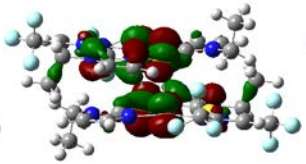
HOMO-12 -0.2838

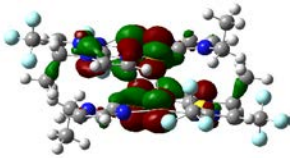
HOMO-13 -0.2851

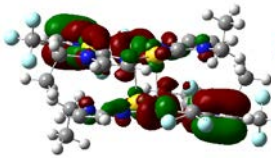
HOMO-14 -0.2867

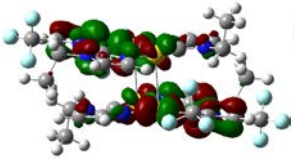
HOMO-15 -0.2873

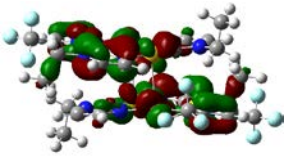
HOMO-16 -0.2884

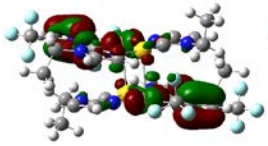
HOMO-17 -0.2887

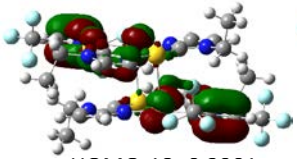
HOMO-18 -0.2901

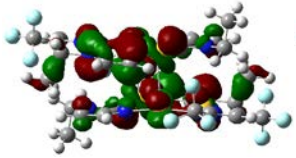
HOMO-19 -0.2901

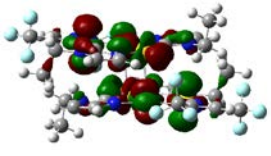
HOMO-20 -0.2941

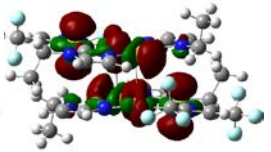
HOMO-21 -0.2942

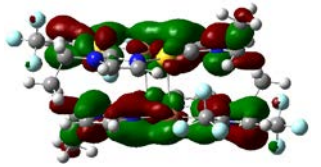
HOMO-22 -0.2981

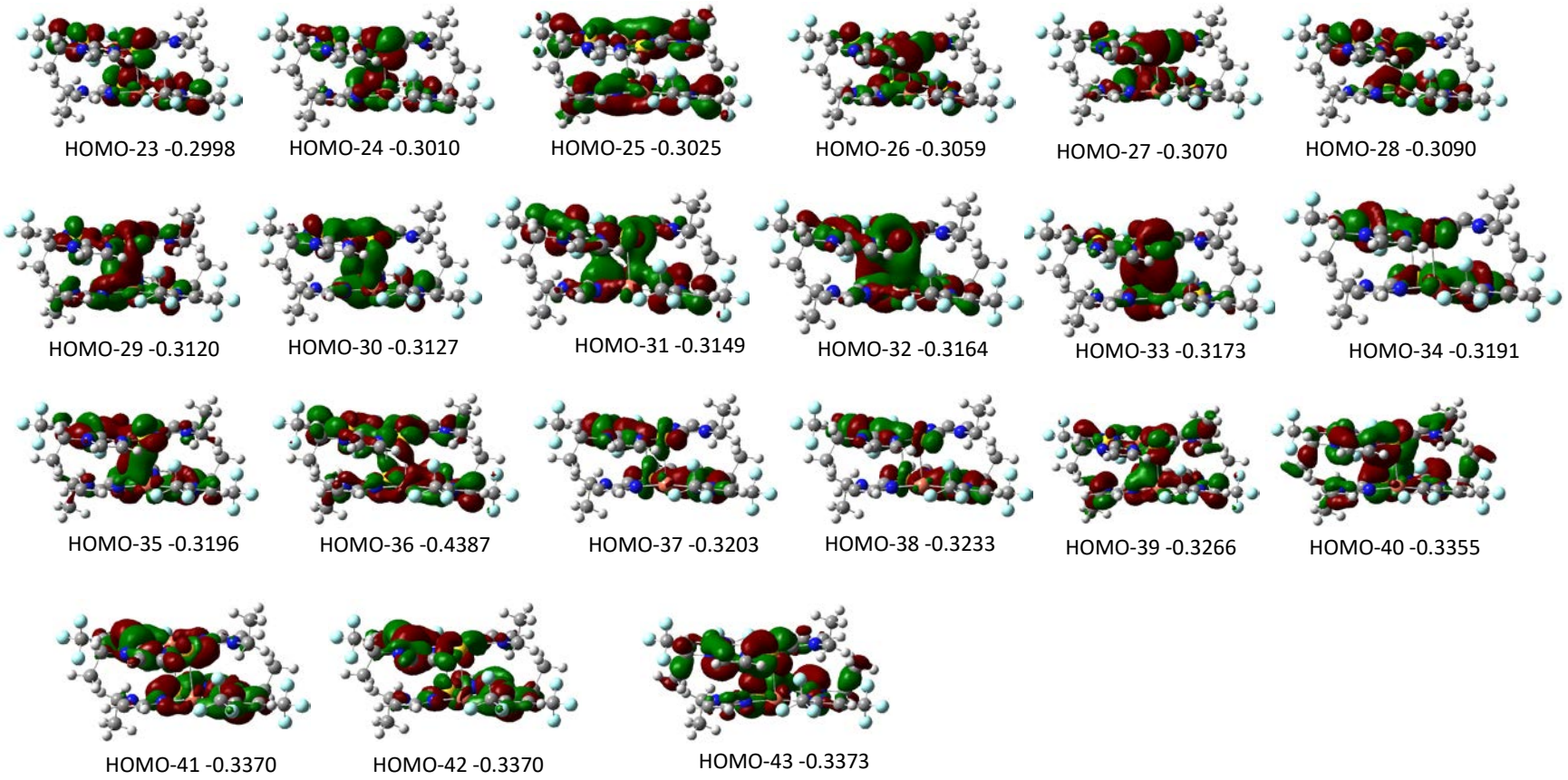

Fig. S6. Kohn-Sham contours of occupied all frontier molecular orbitals (from the HOMO down to HOMO-43) plus the lowest unoccupied molecular orbital (LUMO) in the full $\{[Au_2Im'_2CuPz')]\}_2$ hexanuclear dimer-of-trimer model, where Im' = μ-C^2,N^3-EtIm and Pz' = μ-3,5-$(CF_3)_2$Pz. Orbital energies are taken from DFT computations of the optimized geometry of **4a** shown in **Fig. S2**. Orbital notation is given to describe the relative energy (e.g., H = highest occupied molecular orbital (HOMO); H-41 = the occupied molecular orbital that lies 41st below the HOMO) and absolute energy, given in atomic units next to orbital designations. The isodensity = 0.01 for all orbitals.

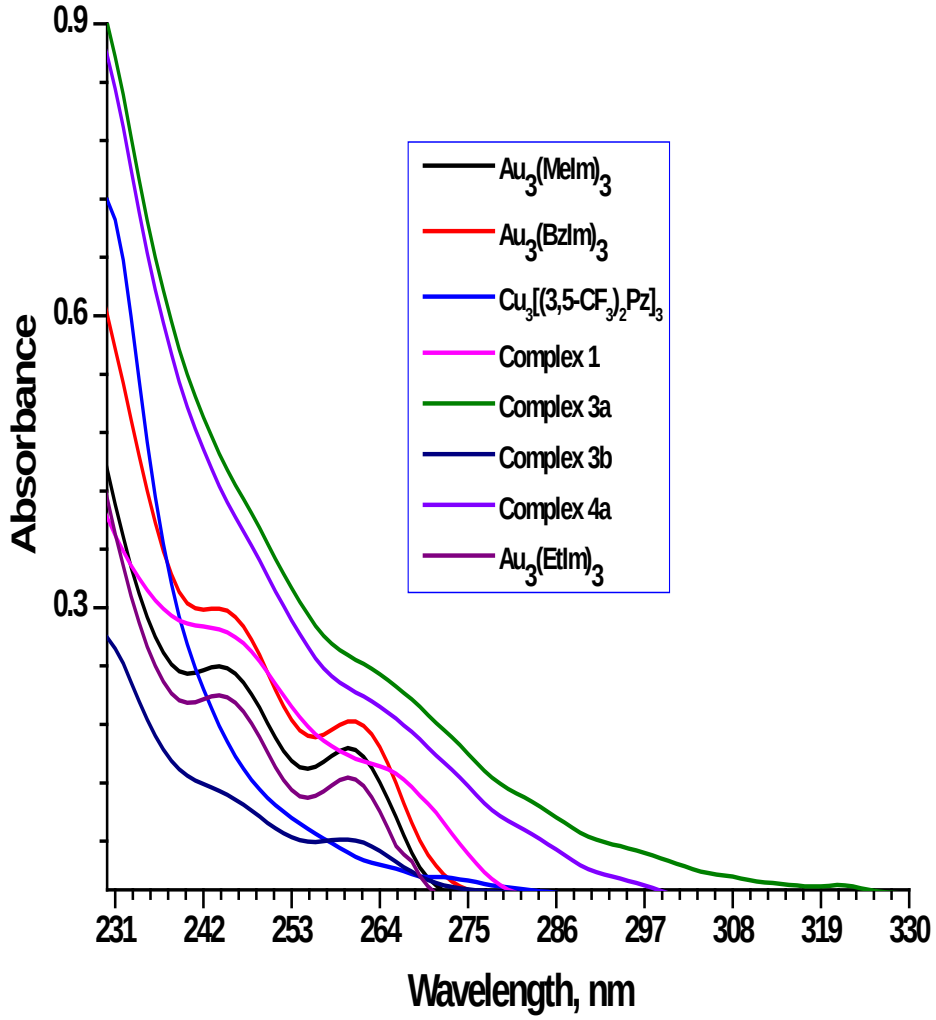

Fig. S7. Absorption spectra of 10^{-5} M dichloromethane solution of starting materials and heterobimetallic complexes.

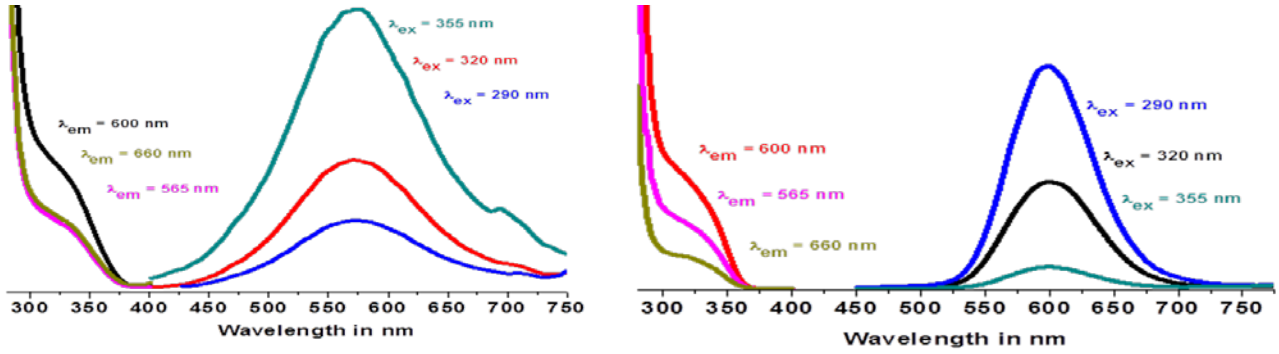

Fig. S8. Photoluminescence spectra for a solid powder sample of $[Au(MeIm)Cu_2((CF_3)_2Pz)_2]$, **3b**, at 298 K (Left) and 77 K (right). Excitation and emission wavelengths used in the emission and excitation spectra, respectively, are labeled on each trace.

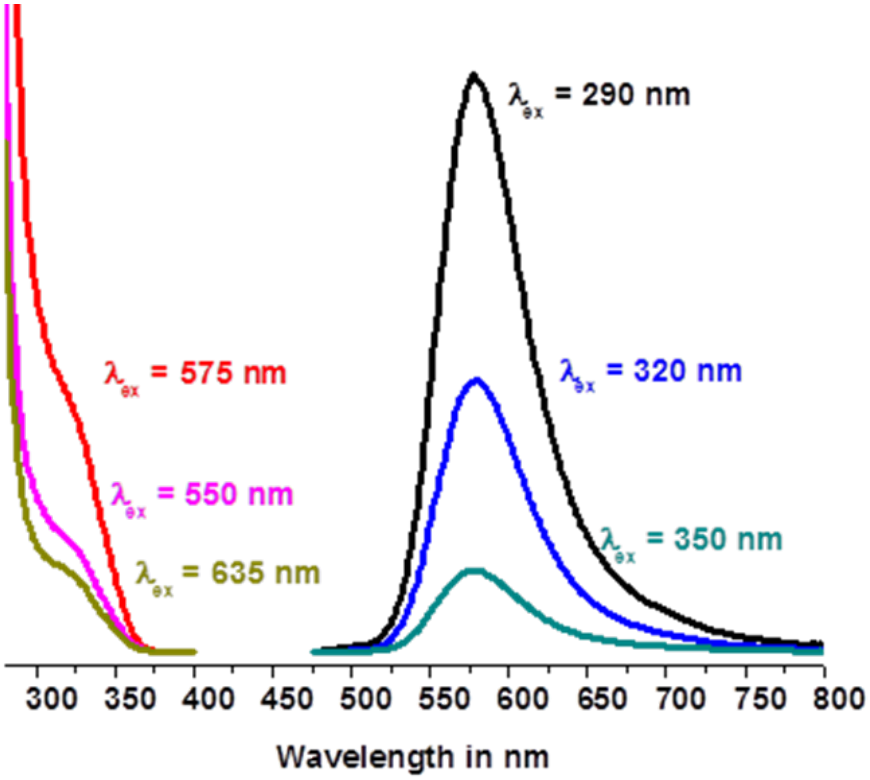

Fig. S9. Shows the steady state photoluminescence for a solid sample of $\{[Au(BzIm)]_3[Cu((CF_3)_2Pz)]_3\}$ at 77 K. Excitation and emission wavelengths used in the emission and excitation spectra, respectively, are labeled on each trace.

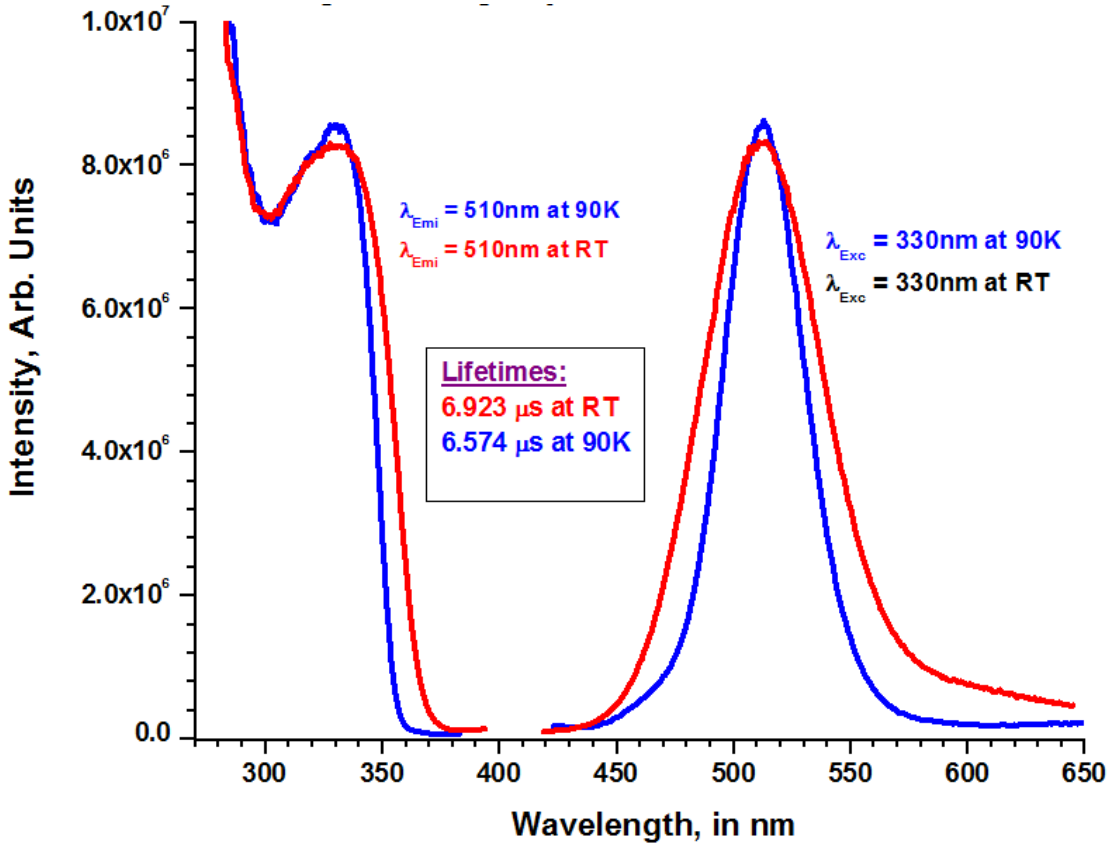

Fig. S10. A comparison of the steady state photoluminescence data (excitation spectra, emission spectra, and lifetimes) at room temperature vs 77 K for a solid sample of **4a**. Excitation and emission wavelengths used in the emission and excitation spectra, respectively, are labeled on each trace. Note the near indifference of emission intensity and lifetime to temperature, consistent with the high Φ_{PL} found for this complex at ambient temperature.

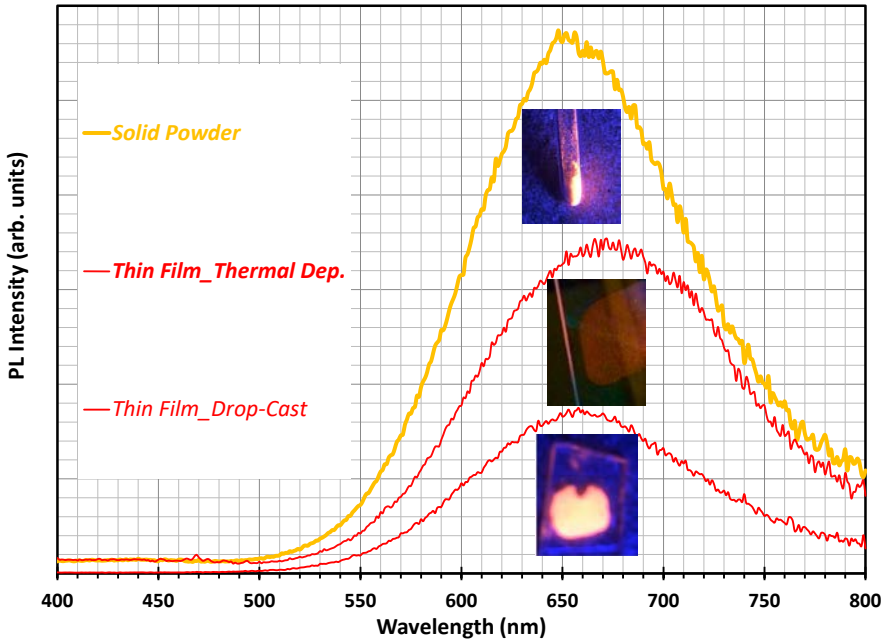

Fig. S11. Demonstration of the processability into OLED functional thin-film forms and the indifference of the photoluminescence spectra thereof *vs* powder forms for $[Cu(\mu\text{-}3,5\text{-}(CF_3)_2Pz)]_3$ at 298K.

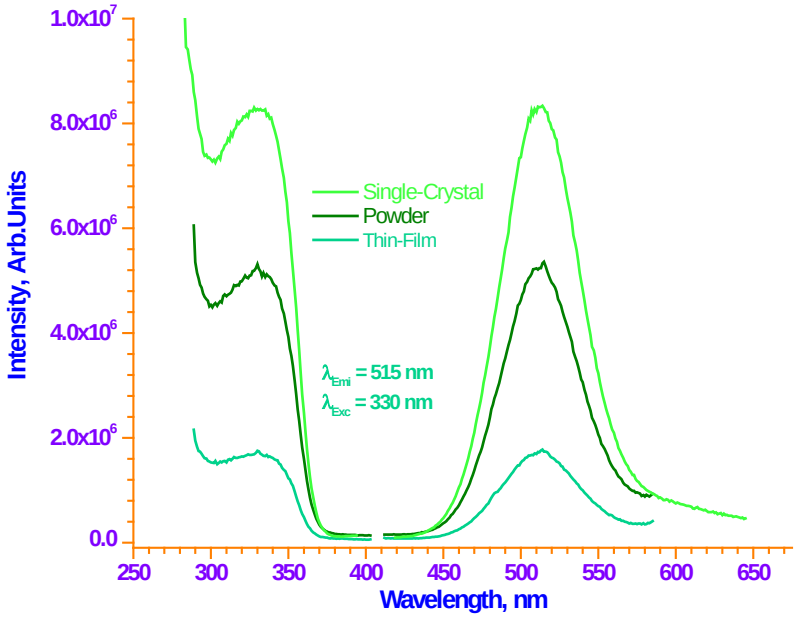

Fig. S12. Demonstration of the processability into OLED functional thin-film forms and the indifference of the photoluminescence spectra thereof *vs* powder and single crystal forms for **4a** at 298K.

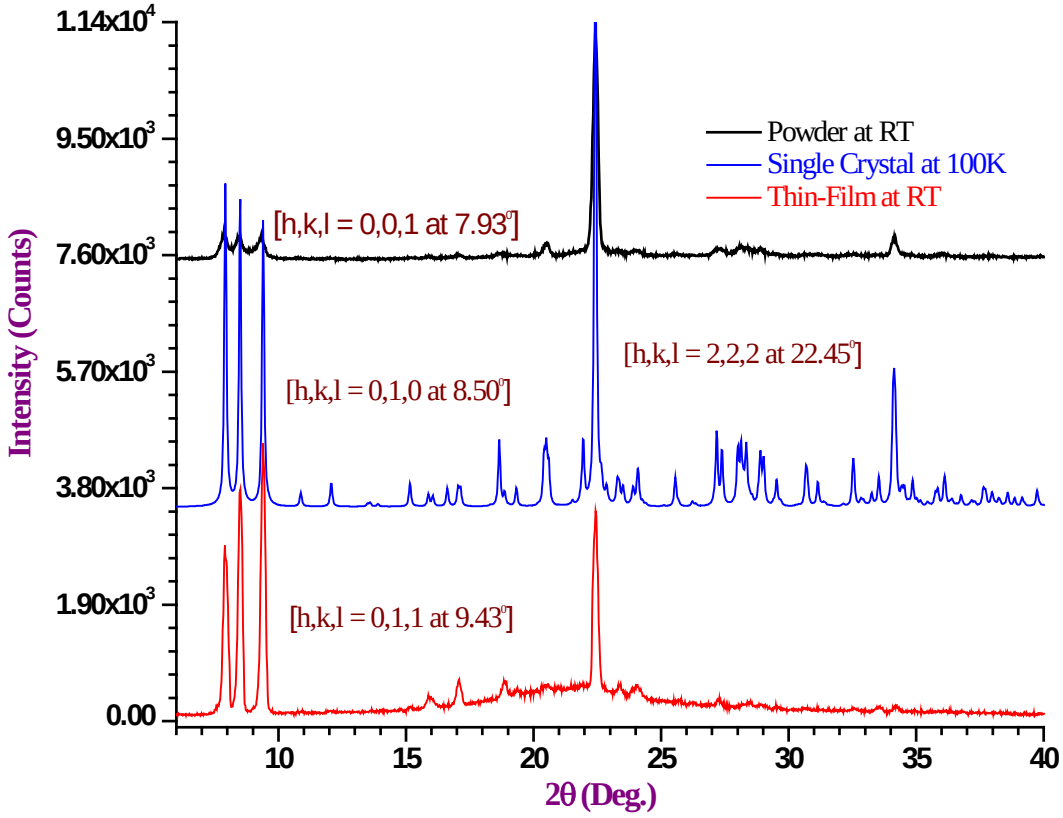

Fig. S13. The XRD patterns of *homometallic* $[Cu(\mu\text{-}3,5\text{-}(CF_3)_2Pz)]_3$. XRD pattern of powder samples on glass substrate(Top), simulated single-crystal powder XRD pattern using Mercury software (middle) and XRD pattern of thin-film prepared by drop-casting method on quartz substrate of dichloromethane solution (Bottom). In the actual powder XRD pattern (Top), the peak at around 22.45 degrees is enhanced while some of the peaks at higher and lower angles are either missing or diminished, demonstrating that the actual powder has preferred orientation of (2,2,2) at around 22.45 degrees. The simulated diffraction pattern of single-crystal data (middle) shows a theoretical data assuming randomly oriented crystallites/particles, thus shows all possible peaks with different faces of all the hkls. The thin film XRD pattern has been enhanced in orientation along the peak at around 9.43 degree (0,1,1). The crystallites usually get more oriented in their preferred direction in a thin film. The broad peak around 21 degrees is the amorphous hump from the quartz substrate.

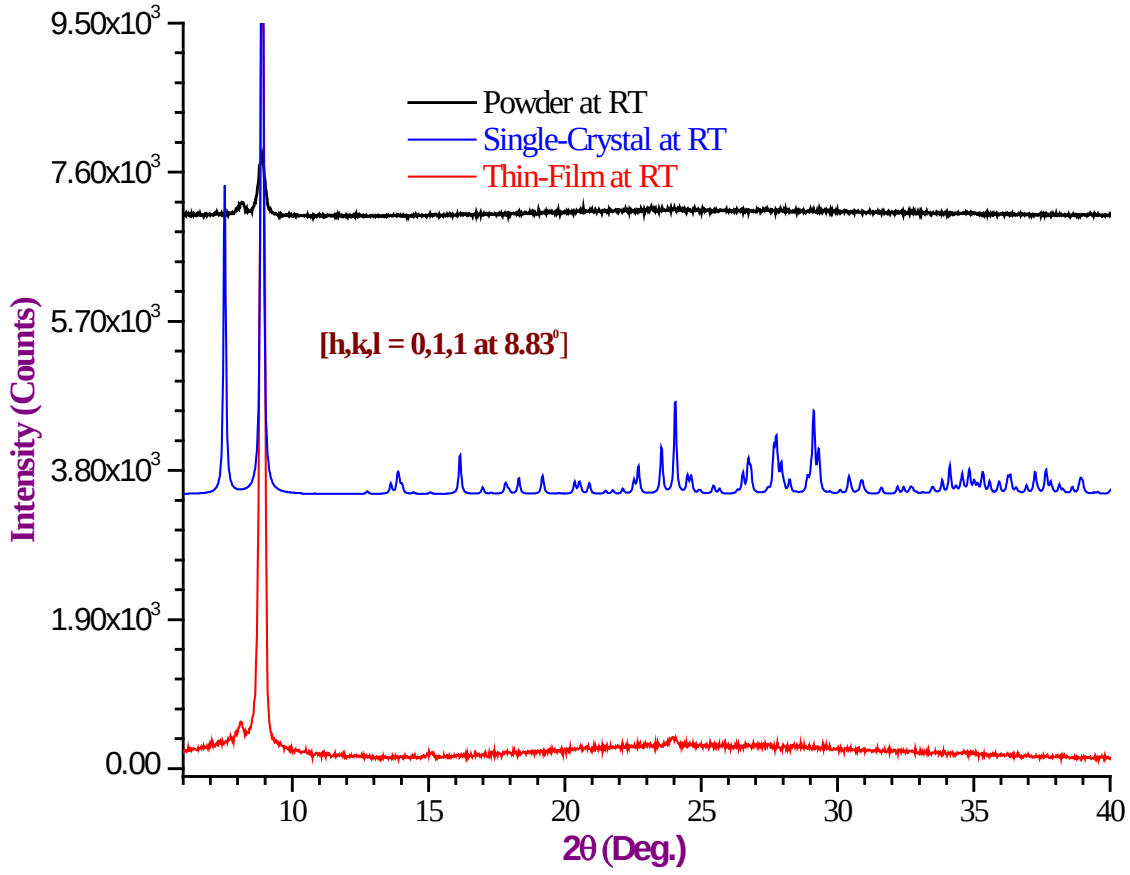

Fig. S14. XRD patterns of *heterobimetallic complex* **4a**. XRD pattern of powder samples on glass substrate (top), simulated single-crystal powder XRD pattern using Mercury software (middle) and XRD pattern of thin-film prepared by drop-casting method on quartz substrate of dichloromethane solution (bottom). In the actual powder XRD pattern (top), the enhanced peak at around 8.83 degrees is demonstrating that the actual powder has preferred orientation along (0,1,1) while some of the peaks at higher angles are either missing or diminished. The simulated diffraction pattern of single-crystal data (middle) shows a theoretical data assuming randomly oriented crystallites/particles, thus shows all possible peaks with different faces of all the hkls. The thin film XRD pattern shows highly enhanced orientation along the peak at around 8.83 degrees (0,1,1) because the crystallites usually get more oriented in their preferred direction in a thin film. The broad peak around 21 degrees is the amorphous hump of the quartz substrate.

References

1. Dias HVR, Polach SA, Wang Z (2000) Coinage metal complexes of 3,5-bis(trifluoromethyl)pyrazolate ligand: Synthesis and characterization of $\{[3,5\text{-}(CF_3)2Pz]Cu\}_3$ and $\{[3,5\text{-}(CF_3)_2Pz]Ag\}_3$. *J. Fluor. Chem.* 103(2): 163-169.
2. Bonati F, Burini A, Pietroni BR, Bovio B (1989) Reactions of C-imidazolyllithium derivatives with group Ib compounds: Tris[μ-(1-alkylimidazolato-N^3,C^2)]tri-gold(I) and -silver(I). Crystal structure of bis(1-benzylimidazolin-2-yliden)gold(I) chloride. *J. Organomet. Chem.* 375(1): 147-160.
3. Sheldrick GM (2015) Crystal structure refinement with SHELXL. *Acta Crystallogr*. C71: 3-8.
4. Sheldrick GM (2008) A short history of SHELX. *Acta Crystallogr*. A64: 112-122.
5. Spek AL (2009) Structure validation in chemical crystallography. *Acta Crystallogr*. D65: 148-155.
6. Cundari TR, Stevens WJ (1993) Effective core potential method for the lanthanides. *J. Chem. Phys.* 98(7): 55555-5565.
7. Stevens WJ, Krauss M, Basch H, Jasien PG (1992) Intramolecular nucleophilic participation by the thiol group during amide hydrolysis. Part 2. The imidazole catalysis dilemma. *Can. J. Chem.* 70(1): 62-67.
8. Zhao Y; Truhlar DG (2008) The M06 suite of density functionals for main group thermochemistry, thermochemical kinetics, noncovalent interactions, excited states, and transition elements: Two new functionals and systematic testing of four M06-class functionals and 12 Other functionals. *Theor. Chem. Acc.* 120(1): 215-241.
9. Zhao Y, Truhlar DG (2008) Density functionals with broad applicability in chemistry. *Acc. Chem. Res.* 41(2): 157-167.